

Spectro-Imaging Polarimetry of the Local Corona During Solar Eclipse

Z.Q. Qu^{1,2}  · G.T. Dun¹ · L. Chang¹ · G. Murray³ ·
X.M. Cheng¹ · X.Y. Zhang¹ · L.H. Deng¹

Received: 1 April 2016 / Accepted: 16 January 2017 / Published online: 14 February 2017
© The Author(s) 2017. This article is published with open access at Springerlink.com

Abstract Results are presented from spectro-imaging polarimetry of radiation from the local solar corona during the 2013 total solar eclipse in Gabon. This polarimetric observation was performed from 516.3 nm to 532.6 nm using a prototype *Fiber Arrayed Solar Optical Telescope* (FASOT). A polarimetric noise level on the order of 10^{-3} results from a reduced polarimetric optical switching demodulation (RPOSD) procedure for data reduction. It is revealed that the modality of fractional linear polarization profiles of the green coronal line shows a diversity, which may indicate complex mechanisms. The polarization degree can approach 3.2 % above the continuum polarization level on a scale of 1500 km, and the nonuniform spatial distribution in amplitude and polarization direction is found even within a small field of view of 7500 km. All of this implies that the coronal polarization is highly structured and complex even on a small scale.

Keywords Polarization · Sun, corona

1. Introduction

The solar corona is the site that hosts most large-scale solar activity, such as solar flares, filament eruptions, and coronal mass ejections (CMEs). Discovering the physical mechanisms that drive these phenomena is at the forefront of solar physics research. However, efforts to reveal such mechanisms are hindered by insufficient understanding of the physical conditions of the solar corona. For example, coronal heating is still an open issue because of our insufficient understanding of the underlying physical processes. Although diagnostic tools such as ultraviolet (UV) and extreme-ultraviolet (EUV) imaging instruments available

✉ Z.Q. Qu
zqqu@ynao.ac.cn

¹ Yunnan Astronomical Observatories, CAS, Kunming, Yunnan 650011, China

² Center for Astronomical Mega-Science, Chinese Academy of Sciences, 20A Datun Road, Chaoyang District, Beijing, 100012, P.R. China

³ Center for Advanced Instrumentation, Durham University, Durham, DH1 3LE, UK

from space-borne telescopes play an increasingly important role, it is clear that polarimetric measurement has become more and more promising for coronal physics research (Dai *et al.*, 2015; de Wijn, Tomczyk, and Burkepile, 2014). On the other hand, observation of the corona is fundamentally more difficult than observations of the other solar atmospheric layers because coronal radiation at the visible (VIS) and infrared (IR) wavelengths is at least six orders of magnitude weaker than that observed from the photosphere. The telluric atmosphere scattering of massively dominant photospheric background makes VIS-IR observation of the corona suffer further from the light pollution for the ground-based coronagraphs. This becomes more serious when polarimetric observation are the aim. Historically, many detailed observations have been conducted during total solar eclipses. Thanks to the heroic efforts of these explorer-scientists, it has been well demonstrated that the much-reduced scattered light from the telluric atmosphere during the obscuration of the solar disk results in a sufficiently reduced background that direct coronal observation becomes briefly possible.

Basically, eclipse coronal polarimetric measurements can be divided into three categories according to their observational functions:

1. Imaging-polarimetry during solar eclipses has a history of more than one hundred years. Most researchers detected highly polarized radiations from the corona and presented highly structured polarization maps (for instance, Ney *et al.*, 1961; Eddy and McKim Malville, 1967; Blackwell and Petford, 1966; Hyder, Mauter, and Shutt, 1968; McDougal, 1971; Koutchmy and Schatten, 1971; Molodensky, 1973; Badalyan and Sýkora, 1997; Kulijanishvili and Kapanadze, 2005; Skomorovsky *et al.*, 2012; Qu *et al.*, 2013). More efficient, improved diagnostic methods (House, 1977; House, Querfeld, and Rees, 1982; Raouafi, Lemaire, and Sahal-Bréchet, 1999; Raouafi, Sahal-Bréchet, and Lemaire, 2002; Raouafi and Solanki, 2003; Raouafi, 2005) have been devised to reveal distributions of electron density, electron temperature, and especially the magnetic field, which is highly relevant here and cannot be accurately diagnosed by non-polarimetric measurements. As is well known, the magnetic field configurations and morphologies play a crucial role in forming coronal features and causing eruptions. It is common knowledge that the linear polarization distribution in the corona is extremely non-uniform. However, various polarimetry measurements differ greatly, as pointed out by Hyder, Mauter, and Shutt (1968). In fact, all these imaging-polarimetries suffer from two fundamental shortcomings. They can neither distinguish the contributions of the continuum from that of the spectral lines within one bandpass, nor can they resolve the situation where linear polarization profiles take on a specific feature of two or more lobes with opposite signs. Because of a lack of spectral detail, it is very difficult to reveal the mechanisms by imaging-polarimetry results.

2. To the best of our knowledge, spectropolarimetry during a solar eclipse was first conducted by a Zurich group, but they failed to extract the polarization profiles (Feller *et al.*, 2007). Subsequently, we performed dual-beam spectropolarimetry during the 2008 total solar eclipse in China (Qu *et al.*, 2009). The fractional linear polarization of emission lines from 502.5 nm to 528.5 nm was detected up to 35.0 % at the Mg I *b*₄ 516.8 nm line with an *rms* polarimetric noise level of 1.6 %. In addition, profiles with close amplitudes of the once-ionized iron lines (Fe II 516.9 nm) and other lines in the upper chromosphere and lower transition region were also recorded. Furthermore, we demonstrated the synoptic consistency between results from spectropolarimetry and imaging-polarimetry, and linear polarization degrees up to 40 % were observed for the magnesium triplet (Mg I *b*₄ 516.8 nm, *b*₂ 517.3 nm and *b*₁ 518.3 nm) and Fe II 516.9 nm with a polarimetric noise level of 4.37 % during the 2010 annular eclipse in China (Qu *et al.*, 2013).

3. The last category, spectro-imaging polarimetry, is presented here for the first time. This was performed during the 2013 total solar eclipse in Gabon with the prototype *Fiber Ar-*

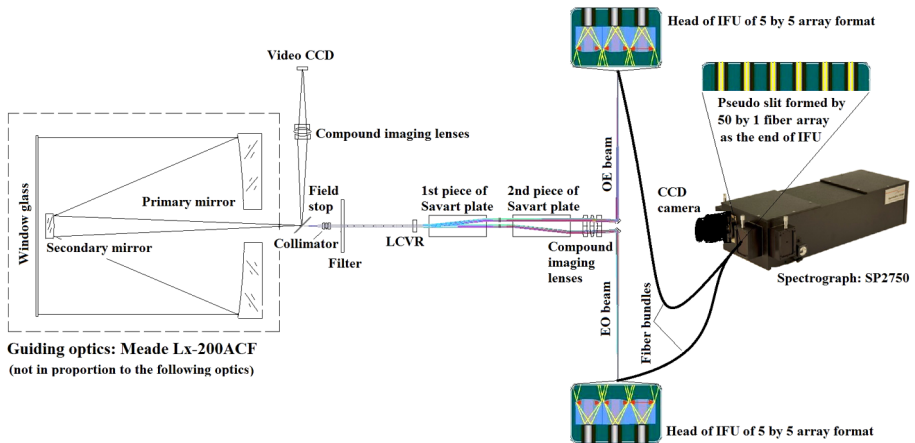


Figure 1 Optical path of the prototype FASOT for solar eclipse polarimetric observation.

rayed Solar Optical Telescope (FASOT, Qu, 2011; Qu *et al.*, 2014). Here the term ‘spectro-imaging polarimetry’ means real-time 2D spectropolarimetry that enables the production of correspondingly reconstructed 2D polarization maps at all the wavelength points within the adopted band of interest.

Finally, it should be noted that the mechanisms producing the polarization have been explored for a long time. For instance, Raouafi (2011) summarized the origin of polarization in K-corona and polarimetric application for diagnosing the coronal magnetic field. The application has also been explored by many authors, reviewed by Raouafi (2005), Trujillo Bueno (2010), and in articles of a special issue entitled ‘Coronal Magnetometry’ in the journal *Frontiers in Astronomy and Space Sciences* published in 2016.

2. Instrumentation and Observation

The prototype FASOT (Qu *et al.*, 2014) achieves real-time 2D spectro-imaging polarimetry of multiple lines by using a pair of integral field units (IFU, *cf.* Allington-Smith *et al.*, 2002) constructed at Durham University CfAI and significantly reduces polarimetric noise levels by applying the polarimetric optical switching (POS) technique (Donati *et al.*, 1990; Bianda, Solanki, and Stenflo, 1998). The optical path of the eclipse observation version is depicted in Figure 1. A Meade LX200-ACF Cassegrain telescope with an aperture of 30 cm was employed as the guiding optics. This was also the optical platform shared by our 2008 and 2010 eclipse observations. A field stop is located at the focal plane that splits the field of view (FOV) into two parts. One smaller part (about 20 arcseconds) passes it directly for the polarimetric measurement, and the remnant FOV is reflected vertically and used for monitoring. A compound collimator and a set of imaging lenses form a telecentric optical system in which the polarimeter sits. Afterward, a polarimeter consists of a filter to block the ultraviolet and shorter wavelength irradiation, a liquid crystal variable retarder (LCVR) used for changing alternatively the polarization states of the two beams that emerge from a Savart plate to execute the POS operation by altering the applied voltage, and the Savart plate serves as the linear polarization analyzer that produces ordinary extraordinary (*oe* for short) and extraordinary ordinary (*eo* for short) beams with equal optical paths, but opposite

polarization states. The first 25 spectra (counted from the top to the bottom) in each panel of Figures 2 and 9 (the raw polarimetric data) are produced by the 'oe' beam in the upper part and the other 25 spectra by the 'eo' beam located in the lower part, and their intensities are defined as Stokes $1/2(I - Q)$ and $1/2(I + Q)$, respectively, in the subsequent analyses. The two beams are separated further by two 45° mirrors and are conducted into two optical arms. On the focal planes of these imaging lenses, a pair of IFUs formed by $2 \times (5 \times 5)$ lenslets and optically coupled fibers are illuminated. At the other end of the IFU pair, the 50 fibers are aligned together in a straight line as a pseudo-slit, and then the emerging light beams are dispersed by a spectrograph PI SP2750. Finally, a CCD camera PI PIXUS400 with pixel format of 1340×400 is placed at the exit focal plane of the spectrograph. It is noteworthy that *oe* and *eo* beams from the Savart plate are tightly related since they have the same solar origin. The two spectra produced by each polarimetric fiber pair, illuminated by the same solar spatial point, but with opposite polarization states, are aligned such that in each panel of Figure 2, which contains fifty spectra, the n th spectrum is coupled symmetrically with the $(51 - n)$ th spectrum counted from top to bottom or *vice versa*. Each fibre illuminates five pixels along the spatial direction (vertical in each panel of Figures 2 and 9), and each pixel covers 0.0122 nm in the dispersion direction (horizontal in Figure 2), and thus the spectral resolution power available from the grating is 21 000, while five pixels along the spatial direction span two arcseconds. Finally, the observational band is adopted from 516.3 nm to 532.6 nm, which contains many photospheric and chromospheric lines including the magnesium triplet, neutral and once-ionized iron lines, as well as the green coronal line.

Because of its mobility and capability of the real-time 2D spectro-imaging polarimetry and thanks to the much reduced polarimetric noise level available compared to our former polarimetries, the prototype FASOT eclipse version is conducted to carry out the coronal polarimetric observation during solar eclipses.

A total solar eclipse took place on November 2, 2013 in Gabon, and a little village named Bifoun ($E0^\circ 17'17'' S10^\circ 29'24''$) was chosen as the observation site within the band of totality. The totality began at 13:56 UT and lasted only one minute. Since the monitoring image was not well resolved, we placed the IFU FOV around the solar crescent formed by lunar occultation. During the entire process, an observation mode was established whereby every acquisition set consisted of six successive images, and they are labeled by $t1$ to $t6$ hereafter. We have acquired enough data sets for different usages. The data assembly contained not only the polarimetric data around and during the totality, but also dark-current and flat-fielding images, as well as polarimetric calibration data sets before and after the totality. The dark current was measured by closing the shutter of the spectrograph with different exposure times. The flat-fielding data were obtained with an exposure time of 50.0 seconds by illumination from an artificial white-light source placed in front of the telescope after the totality (see panel (b) of Figure 2). The top panel of Figure 2 shows the spectra of the quiet-Sun region close to solar disk center acquired before the eclipse, which is used for wavelength calibration and spectral line identification (the representative lines are labeled by their elements and ionization stages at the top). The two bottom panels of Figure 2 show the first and second frames of the data set 'Cali0_end.spe' when the transmission direction of the HN45 polaroid was placed just before the window glass in the north-south direction defining positive Stokes Q , consistent with the polarization plane direction of 'eo' beam and in negative Stokes Q direction, respectively. They are used as the reference data for the proposed demodulation procedure introduced below. Four similarly obtained polarimetric calibration data sets were acquired after the eclipse, but they are not shown here.

The coronal polarimetric measurement with only the green line present in the observing band was recorded in the latter four frames of the data set and was named 'se205.spe', and all

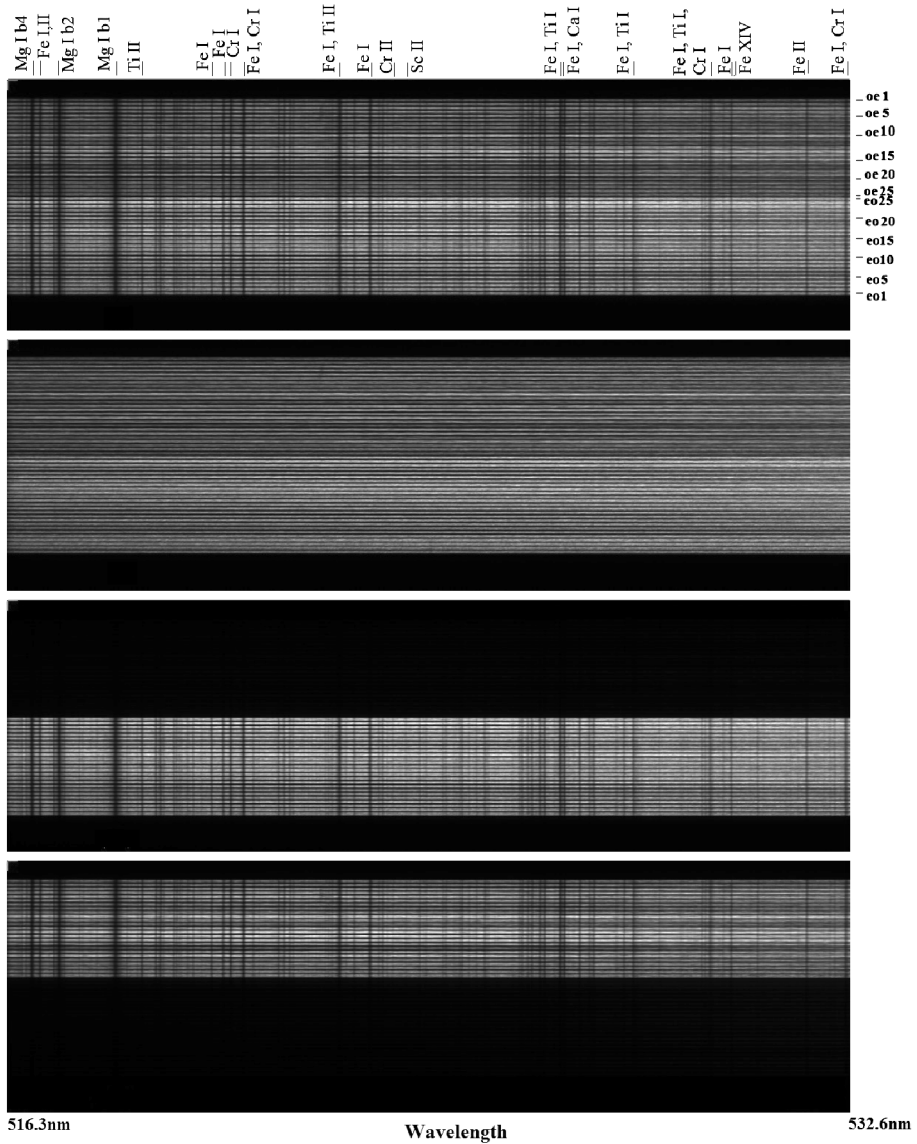


Figure 2 Sample raw images for wavelength, flat-fielding and polarimetric demodulation reference data. The observational band spans from 516.3 nm to 532.6 nm. The important spectral lines are labeled by their corresponding elements and ionization stages at the top. Note that in each panel intensities of the upper 25 spectra are $1/2(I - Q)$ produced by oe pairs and those of the lower 25 spectra are $1/2(I + Q)$ by eo pairs. The alignment of fiber pairs in the slit (spatial direction) is labeled near the right of the top panel and the same for the others. The top panel was acquired before the eclipse near the disk center using a tiny fractional aperture. The second (counted from the top to the bottom, and hereafter) was acquired by illumination of artificial white light as flat-field image. The third and fourth panels were acquired with polarization states exchanged, which are used as the two successive reference frames for data reduction of reduced polarimetric optical switching demodulation (RPOSD, hereafter).

the frames of sets ‘se206.spe’ and ‘se207.spe’ during the totality. These form the samples of the polarimetric measurement in the outer corona. The green coronal line was also recorded along with other lines in many frames of data sets, however, such as ‘se204.spe’ and the first two frames of ‘se205.spe’. All these data form the assembly to be demodulated for our following analysis.

3. Data Reduction

Polarimetric observation, especially spectropolarimetry, during a total solar eclipse is a great challenge. It requires not only mobility of the suitable instrument, good weather condition and sufficient logistics, but also a suitable strategy of compromise between the temporal resolution and the signal-to-noise ratio, since only a very short observation time is available. Otherwise, suitable calibration data acquisitions should be carried out before and after the totality.

Following the usual procedure, the dark currents for the polarimetric data and the flat-fielding were subtracted, which was followed by the normal flat-fielding operation. Because each lenslet-coupled fiber of IFU represents a spatial resolution element and illuminates five pixels along the spatial direction (vertical in each panel of Figures 2 and 9), we combined these five pixels into one at each wavelength, *i.e.*, a 5×1 binning was executed after the dark-current and flat-fielding calibration.

The real challenge in data reduction is in the demodulation procedure since the photon budget is not enough, therefore the polarimetric noise level should be sufficiently depressed in a special way. In our case, this is a complicated situation since the traditional polarimetric optical switching demodulation (POSD) cannot directly result in lower polarimetric noise level (see Figure 4) by numerical test. We had to figure out a new demodulation method to sufficiently lower the level. In the following, we describe this newly developed procedure.

The intensities of the dual beams received by ‘oe’ and ‘eo’ pixels labeled $(x1, y1)$ and $(x2, y2)$, respectively, can be expressed by at time t ,

$$\begin{aligned} I_{\text{obs,oe}}(t) &= 1/2 [I_{\text{sun}}(t) - Q_{\text{sun}}(t)] g_{(x1,y1)} s(t), \\ I_{\text{obs,eo}}(t) &= 1/2 [I_{\text{sun}}(t) + Q_{\text{sun}}(t)] g_{(x2,y2)} s(t), \end{aligned} \quad (1)$$

where I_{sun} represents the radiative intensity from the Sun, and Stokes Q_{sun} is the linear polarization intensity. Term $g_{(x_i, y_i)}$ is a quantity reflecting the instrumental efficiency of collecting the photons from the Sun along a specific optical path onto the relevant chip pixel. It varies from one light path to another and reflects the non-solar spatial variation of the instrument, such as transparency differences between the dual beams and the gain variations of the detector chip pixels; term $s(t)$ encompasses temporal variations, such as seeing fluctuation. The fractional linear polarization Q/I from the direct demodulation of the dual-beam polarimetry (DBP) is simple and straightforward:

$$\begin{aligned} Q_{\text{sun}}/I_{\text{sun}}(t) &= [g_{(x1,y1)}/g_{(x2,y2)} I_{\text{obs,eo}}(t) - I_{\text{obs,oe}}(t)] \\ & \quad / [g_{(x1,y1)}/g_{(x2,y2)} I_{\text{obs,eo}}(t) + I_{\text{obs,oe}}(t)]. \end{aligned} \quad (2)$$

Evidently, this quantity is strongly influenced by the spatial nonuniformity, *i.e.*, $g_{(x1,y1)}/g_{(x2,y2)} \neq 1$ while the influence from the temporal variation is minimized. Therefore instrumental spatial non-uniformity becomes the main error source and unfortunately causes a high polarimetric noise level for the direct DBP demodulation.

In polarimetric literature, in order to depress the noise level, the POS operation and corresponding demodulation was proposed by Donati *et al.* (1990), and then developed by other authors (*e.g.*, Bianda, Solanki, and Stenflo, 1998). The operation aims at simultaneously minimizing the influence from both non-solar temporal and spatial variations that are due to the weather and the instrument imperfectness during the modulation process. Traditionally, the POS is performed by exchanging the opposite polarization states of the dual beams. For instance, after the acquisition at t , another measurement at time t' is required, which results in the intensities $I_{\text{obs,oe}}$ and $I_{\text{obs,eo}}$ of the two beams,

$$\begin{aligned} I_{\text{obs,oe}}(t') &= 1/2[I_{\text{sun}}(t') + Q_{\text{sun}}(t')]g_{(x1,y1)}S(t'), \\ I_{\text{obs,eo}}(t') &= 1/2[I_{\text{sun}}(t') - Q_{\text{sun}}(t')]g_{(x2,y2)}S(t'). \end{aligned} \quad (3)$$

Following Donati *et al.* (1990) to construct a function f of wavelength from the two measurements at time t and t'

$$f = [I_{\text{obs,oe}}(t)I_{\text{obs,eo}}(t')]/[I_{\text{obs,eo}}(t)I_{\text{obs,oe}}(t')], \quad (4)$$

it is easily demonstrated after several algebraic steps that

$$(\sqrt{f} - 1)/(\sqrt{f} + 1) = Q_{\text{sun}}/I_{\text{sun}}(t) + Q_{\text{sun}}/I_{\text{sun}}(t'), \quad (5)$$

if

$$abs(Q_{\text{sun}}/I_{\text{sun}}(t) - Q_{\text{sun}}/I_{\text{sun}}(t')) \ll 1.0. \quad (6)$$

Alternatively, according to Bianda, Solanki, and Stenflo (1998),

$$(f - 1)/(f + 1) = Q_{\text{sun}}/I_{\text{sun}}(t) + Q_{\text{sun}}/I_{\text{sun}}(t'), \quad (7)$$

when the condition (6) stands again.

In these two ways, we obtain $Q_{\text{sun}}/I_{\text{sun}}(t, t') = 1/2(Q_{\text{sun}}/I_{\text{sun}}(t) + Q_{\text{sun}}/I_{\text{sun}}(t'))$ as the average over the time interval (t, t') . It is noteworthy that in order to obtain the average, this kind of POS demodulation (POSD, and hereafter) procedure requires twofold measurements at the expense of the temporal resolution for the same Stokes parameter combination. If this procedure continues to be executed in the following polarimetry, the measurement time will be twice longer than the polarimetry without POS operation.

In our case, the dual beams are produced by the Savart plate and the polarization state exchange task is assigned to the LCVR. When the above POSD is directly applied to these data sets, it is found that the noise depression is not satisfied, as shown in Figure 4. On the other hand, according to the following numerical experiment, when a modified POSD is created, we find that these data sets obtained by POS operation at the end of eclipse can be treated as the reference data to obtain more satisfactory results.

Now we describe this in detail. The intensities of the dual beams of polarimetry at t_i can be written as

$$\begin{aligned} I_{\text{obs,oe}}(t_i) &= 1/2[I_{\text{sun}}(t_i) - Q_{\text{sun}}(t_i)]g_{(x1,y1)}S(t_i), \\ I_{\text{obs,eo}}(t_i) &= 1/2[I_{\text{sun}}(t_i) + Q_{\text{sun}}(t_i)]g_{(x2,y2)}S(t_i). \end{aligned} \quad (8)$$

The POS polarimetries at t and t' whose intensities are expressed by Equation (1) and Equation (3) are treated as the reference data. Following the same steps as Bianda, Solanki, and Stenflo (1998), if condition (6) is satisfied and also stands for $Q_{\text{sun}}(t_i)/I_{\text{sun}}(t_i)$, then we have from Equation (1) and Equation (8)

$$(f_1 - 1)/(f_1 + 1) = Q_{\text{sun}}/I_{\text{sun}}(t_i) - Q_{\text{sun}}/I_{\text{sun}}(t), \quad (9)$$

and from Equation (3) and Equation (8)

$$(f_2 - 1)/(f_2 + 1) = Q_{\text{sun}}/I_{\text{sun}}(t_i) + Q_{\text{sun}}/I_{\text{sun}}(t'), \tag{10}$$

where

$$\begin{aligned} f_1 &= [I_{\text{obs,co}}(t_i)I_{\text{obs,oe}}(t)]/[I_{\text{obs,oe}}(t_i)I_{\text{obs,co}}(t)], \\ f_2 &= [I_{\text{obs,co}}(t_i)I_{\text{obs,oe}}(t')]/[I_{\text{obs,oe}}(t_i)I_{\text{obs,co}}(t')]. \end{aligned} \tag{11}$$

The sum of Equation (9) and Equation (10) results in

$$Q_{\text{sun}}/I_{\text{sun}}(t_i) = 0.5[(f_1 - 1)/(f_1 + 1) + (f_2 - 1)/(f_2 + 1)], \tag{12}$$

if the time difference between t and t' is so short that

$$Q_{\text{sun}}/I_{\text{sun}}(t) = Q_{\text{sun}}/I_{\text{sun}}(t'). \tag{13}$$

Again, by following Donati *et al.* (1990), we theoretically have an alternative expression if condition (13) is strictly satisfied

$$Q_{\text{sun}}/I_{\text{sun}}(t_i) = (\sqrt{f_1 f_2} - 1)/(\sqrt{f_1 f_2} + 1). \tag{14}$$

Evidently, from either Equation (12) or Equation (14), like Equation (5) and Equation (7), the influence from $g(x_i, y_i)$ and $s(t)$ is theoretically minimized. Because this kind of demodulation is based on the POS performance, we call it reduced polarimetric optical switching demodulation (RPOSD, hereafter).

Generally, condition (13) can be satisfied for fast successive acquisition when the POS is applied for the same region if the LCVR retardation exchange was exactly from 0° to 180° . However, in a general case, the second measurement of the POS performance was not so perfect because the retardation of 180° by the LCVR cannot be perfectly achromatic in the band of interest. Therefore, a small but non-negligible error makes condition (13) read approximately $Q_{\text{sun}}/I_{\text{sun}}(t') = Q_{\text{sun}}/I_{\text{sun}}(t) + c$, with c a small quantity that varies with wavelength. This causes Equation (12) and Equation (14) to have an additional polarization with the same order of c .

For RPOSD, the selection of the reference data obtained by POS operation is very important to serve the purpose of depressing the noise level. After numerical experiments and comparisons, the additional polarimetric calibration data are found to be most suitable. However, in order to use these data, we have to do some modifications since the polarization degrees induced by the polaroid are close to 100.0 %. Because these reference frames were obtained with transmission direction of the HN45 polaroid parallel to the direction defining the positive Stokes Q , the linear polarization degree of the polaroid Q/I is expressed as

$$Q/I = 1 - Q_0/I_0. \tag{15}$$

The upper panel in Figure 3 shows the measurement for Q_0/I_0 to be around 3.5 %. It is shown that the Q_0/I_0 is demodulated to be neither uniformly distributed along the dispersion direction nor in the spatial direction by the POSD. It is evident that the condition

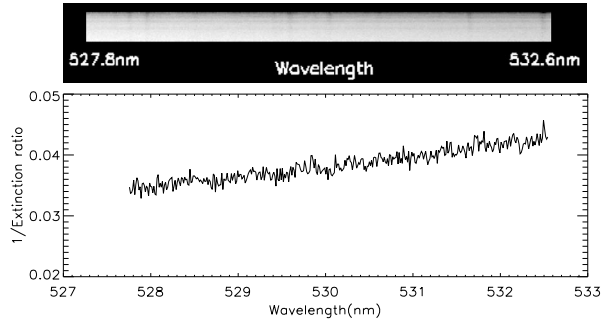
$$Q_{\text{sun}}/I_{\text{sun}}(t_i) \times Q_0/I_0 \ll 1.0, Q_{\text{sun}}/I_{\text{sun}}(t_i), \text{ or } Q_0/I_0 \tag{16}$$

is easily satisfied since $Q_0/I_0, Q/I(t_i) \ll 1.0$ in general.

Now, it becomes possible to define measurable quantities

$$f_3 \equiv \frac{I_{\text{obs,oe}}(t) \times I_{\text{obs,co}}(t_i)}{I_{\text{obs,co}}(t) \times I_{\text{obs,oe}}(t_i)}, \quad f_4 \equiv \frac{I_{\text{obs,oe}}(t') \times I_{\text{obs,co}}(t_i)}{I_{\text{obs,co}}(t') \times I_{\text{obs,oe}}(t_i)}. \tag{17}$$

Figure 3 Wavelength variation of Q_0/I_0 of the polaroid defined in the text. Upper panel: Q_0/I_0 image. Lower panel: sample Q_0/I_0 profile drawn from the upper panel image.



Substituting Equation (1), Equation (8), and Equation (15) into the above equation, we have

$$f_3 = \frac{Q_0/I_0(1 + Q_{\text{sun}}/I_{\text{sun}}(t_i))}{(2 - Q_0/I_0)(1 - Q_{\text{sun}}/I_{\text{sun}}(t_i))}. \tag{18}$$

Expanding the denominators and numerators and dropping the product $Q_{\text{sun}}/I_{\text{sun}}(t_i) \times Q_0/I_0$ according to Equation (16), the above equation is reduced to

$$f_3 = \frac{Q_0/I_0}{2(1 - Q_{\text{sun}}/I_{\text{sun}}(t_i)) - Q_0/I_0} \tag{19}$$

or

$$1 + 1/f_3 = \frac{2(1 - Q_{\text{sun}}/I_{\text{sun}}(t_i))}{Q_0/I_0}. \tag{20}$$

Similarly, substituting Equation (3), Equation (8), and Equation (15) into Equation (17) and considering Equation (16) after several steps leads to

$$1 + f_4 = \frac{2(1 + Q_{\text{sun}}/I_{\text{sun}}(t_i))}{Q_0/I_0}. \tag{21}$$

Then we have from the above equations

$$Q_{\text{sun}}/I_{\text{sun}}(t_i) = (g - 1)/(g + 1) + O(Q_{\text{sun}}/I_{\text{sun}}(t_i) \times Q_0/I_0), \tag{22}$$

regardless of Q_0/I_0 , and

$$g \equiv (1/f_3 + 1)/(f_4 + 1). \tag{23}$$

In Equation (22), the term $O(Q_{\text{sun}}/I_{\text{sun}}(t_i) \times Q_0/I_0)$ represents the remnant error by dropping those terms containing $Q_{\text{sun}}/I_{\text{sun}}(t_i) \times Q_0/I_0$.

In order to test the polarimetric noise levels reduced by the POSD and RPOSD in our case and to view the polarimetric behaviors of the different fiber pairs, we demodulated the data acquired in the quiet-Sun region after the eclipse (shown in the top panel of Figure 2). The Stokes I and Q/I spectral images demodulated by RPOSD and POSD are plotted in the upper panel of Figure 4. It is immediately seen that the noise level reduced by RPOSD in Q/I image is much lower than that by POSD, as is more clearly seen in the lower panel where sample profiles are plotted. Because of these numerical experiment tests, we employ RPOSD expressed by Equation (22) below.

Finally, the modification of the incoming Stokes $(Q/I)_{\text{sun}}$ caused by the instrument systematically is described by Mueller formalism (for coronal polarimetry, Stokes V/I can be ignored)

$$(Q/I)_{\text{obs}} = [M_{21} + M_{22}(Q/I)_{\text{sun}} + M_{23}(U/I)_{\text{sun}}]T, \tag{24}$$

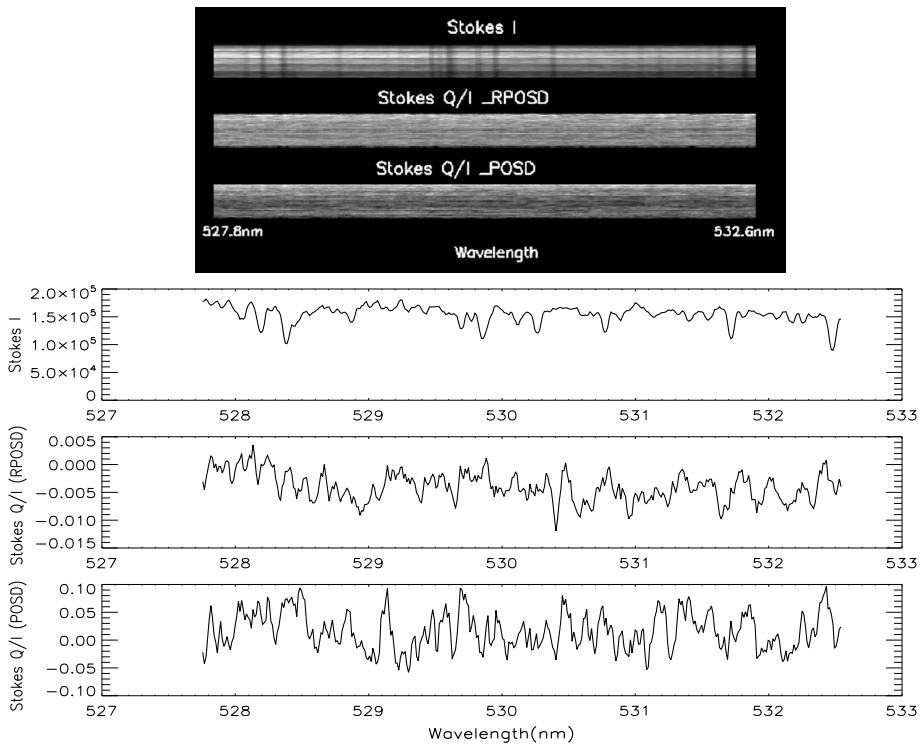


Figure 4 Demodulated Stokes I and Q/I spectral images (upper panel) and corresponding sample profiles demodulated from the 19th pair via respectively the RPOSD and POSD (the lower panel) in a quiet-Sun region. RPOSD can clearly decrease the noise better than the normal polarimetric optical switching (POSD).

where T indicates transparency, and $M_{21}T$ reflects the crosstalk from Stokes I to Q , which is generally a very small quantity (measured from 2.47×10^{-3} to 8.74×10^{-3} within the green coronal line for these 25 polarimetric pairs). $M_{22}T$ reflects the polarimetric efficiency for Stokes Q/I . It is calculated to range from 9.36×10^{-1} to 9.72×10^{-1} for these polarimetric pairs, while $M_{23}T$ indicates the crosstalk from Stokes U/I to Q/I , which is found to be from -9.07×10^{-2} to -1.10×10^{-1} . The polarimetric calibration is executed pair by pair at each wavelength according to Equation (24). Because we did not undertake a Stokes U measurement, the polarimetric calibration of the crosstalk from U/I to Q/I cannot be completed. This should not critically influence the resulting profiles in most cases, however, since the coefficients are so small.

In order to determine the polarimetric behavior of the 25 pairs in the quiet-Sun case, we depict Q/I profiles from Figure 5 to Figure 8, along with that produced by the 19th pair shown in Figure 4. The polarimetric noise level measured over the whole band as the root mean square (*rms*) ranges from 2.18×10^{-3} at the 12th pair to 6.66×10^{-3} at the 25th pair for all the pairs, with an average noise level of 3.16×10^{-3} over all the 25 pairs. It is noteworthy that for the data acquired around totality, the noise level was reduced since the scattering by Earth's atmosphere was significantly reduced.

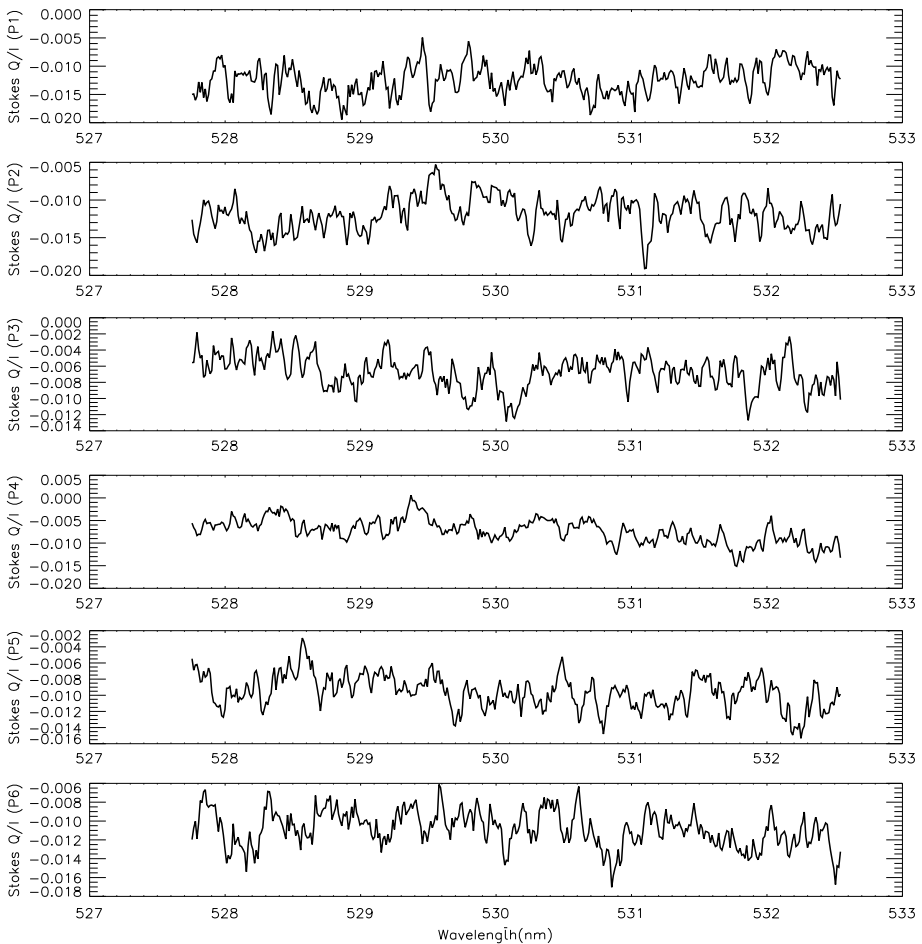


Figure 5 Polarimetric noise level samples demodulated via the RPOSD from the 1st to 6th pairs.

4. Results from Polarimetric Observations of the Local Solar Corona

In this section, we first present the polarimetric results of the inner corona and then those of the outer corona demodulated from the RPOSD described by Equation (22). The two regions are distinguished here by their spectral spatial distribution feature. In the inner corona, not only the coronal line, but also the chromospheric lines are observable, while in the outer corona, only the green coronal line can be observed in the band, and even the continuum is merged in the noise. Panels (a) and (b) of Figure 9 present the raw polarimetric data of the first case. They are selected from the first and second frames of the data set ‘se205.spe’ acquired only several seconds earlier than the second contact with an exposure time of six seconds. Hereafter we call these two frames inner coronal sample 1 (ICS1) and inner coronal sample 2 (ICS2). The amazing observational fact is the coexistence of the coronal, chromospheric, and even photospheric lines in the same FOV, and their intensities are comparable in some spatial points. Especially the Fe I, Fe II, and Fe XIV lines are present simultaneously in the form of emission lines. This may signify that there exists a cool component yielding

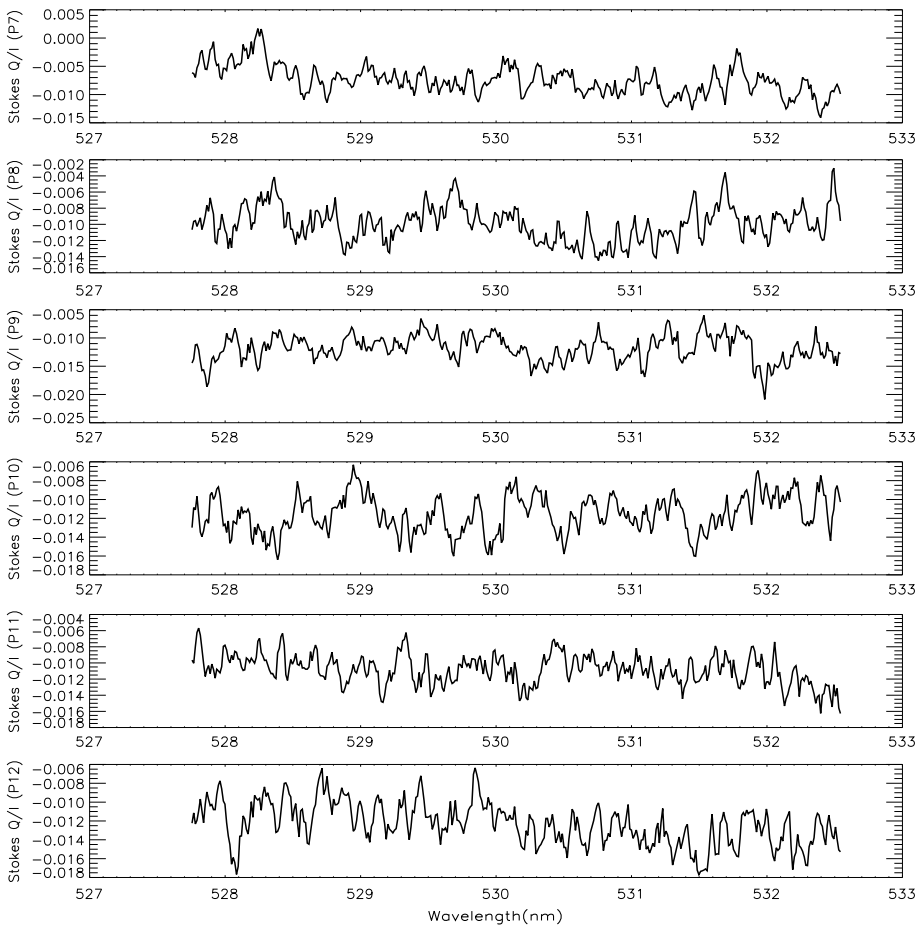


Figure 6 Polarimetric noise level samples demodulated via the RPOSD from the 7th to 12th pairs.

these neutral and singly ionized lines in the inner corona, and we leave this topic to another article. We note that in case (b), the green line produced in some points is nearly as intense as the chromospheric lines (*e.g.* the magnesium triplet or the singly ionized iron lines). Panels(c) and (d) display the typical polarimetric data in the outer corona where only the green coronal line is observable, and even the continuum intensity is beyond the detection limit. They are chosen from the third frame of the data set ‘se205.spe’ and the first frame of ‘se206.spe’ acquired during the totality when the exposure time was adjusted to be eight seconds. They are hereafter named OCS1 and OCS2 for short, respectively.

Since we focus on coronal polarimetry, only the green coronal line and its surrounding spectral lines ranging from 527.8 nm to 532.6 nm are concerned in the discussions below.

4.1. Results from Polarimetric Observations of the Local Inner Corona

The polarimetric results of ICS1 and ICS2 are shown in the upper and lower panels of Figure 10, respectively. A strong contrast is visible in the two demodulated Q/I images: no significant polarization signal could be detected in ICS1, even the spectral intensities

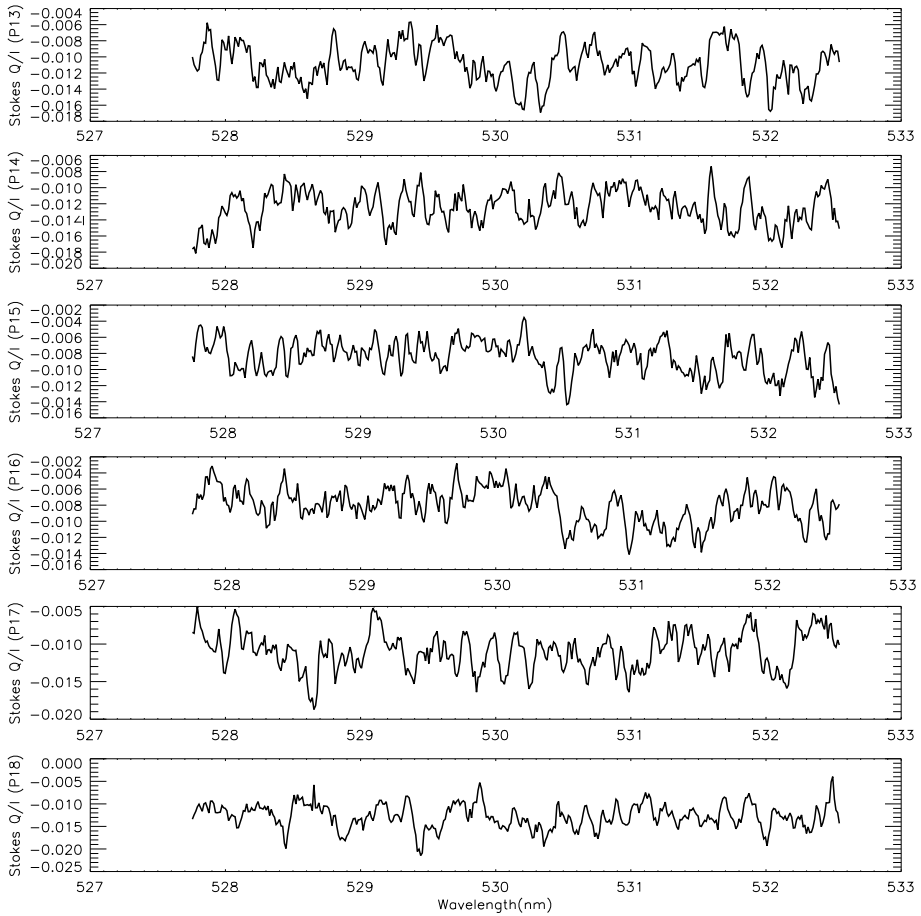


Figure 7 Polarimetric noise level samples demodulated via the RPOSD from the 13th to 18th pairs.

are much stronger than ICS2, while an outstanding polarization signal is detected in ICS2. Another contrast we found is that the additional polarizations due to scattering that appeared in the last five pairs become much weaker in ICS2 than in ICS1, since ICS2 was acquired closer to the totality.

The Stokes I and Q/I profiles of the 7th, 11th, and 13th pairs drawn from the lower panel of Figure 10 (*i.e.* ICS2 case) are plotted in Figure 11, and those of the 14th, 16th and 23rd pairs are depicted in Figure 12. The most markable feature in these profiles is the morphological abundance. We can see a single-valley-dominated profile yielded by pair 13, profiles with two peaks (valleys) with one significant valley (peak) between produced by pairs 11, 14, 16, and 23, and even complex profiles with multiple lobes are found from pair 7. We found amplitudes larger than 1.0 % above the continuum polarization level. For instance, the maximum Q/I amplitude approaches 1.9 % above the continuum in the 23rd pair (the bottom panel in Figure 12). Another feature is revealed: in some spatial points, the amplitudes can hardly be seen above the noise level at the lines. For instance, for pairs 9 and 10, no signal above the noise level is detected. This reflects the non-uniform feature of the polarization distribution, even in this small FOV of 10 arcseconds. We note that the average

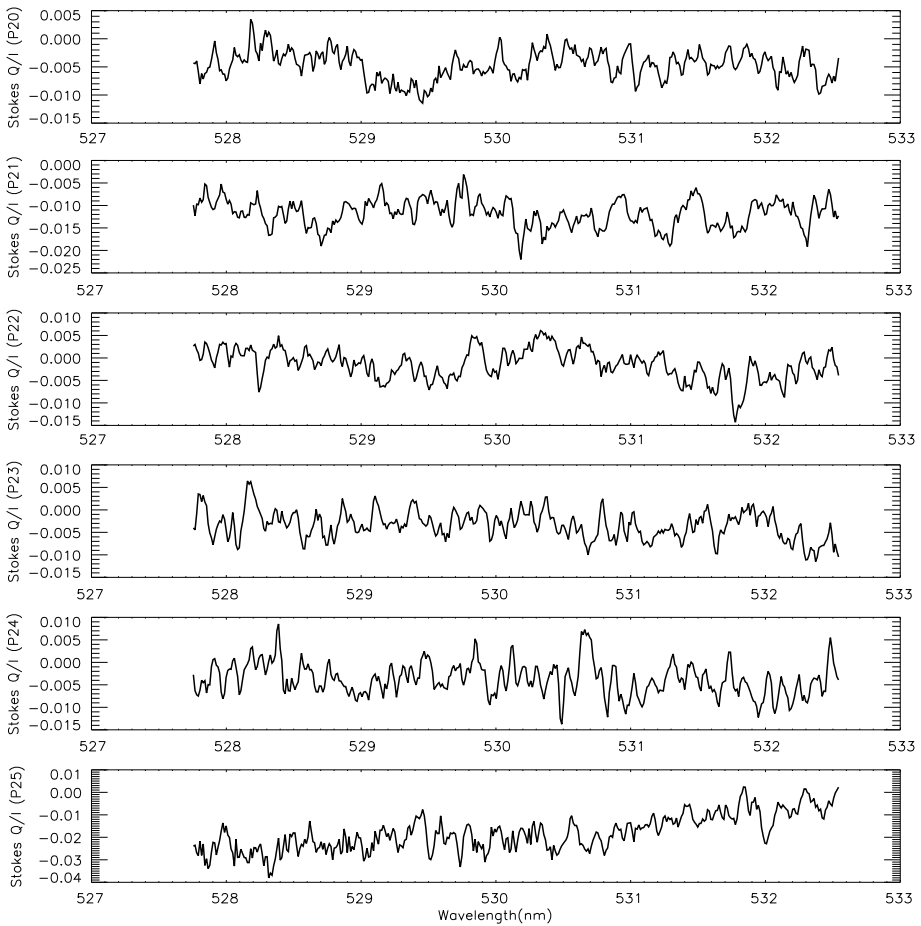


Figure 8 Polarimetric noise level samples demodulated via the RPOSD from the 21st to 25th pairs.

polarimetric noise level over the 25 pairs reads 1.59×10^{-3} in this measurement. Finally, the continuum polarization level in all the cases is located at about -0.74% .

The corresponding Stokes I and Q/I maps of the green coronal line and Fe II 531.7 nm for ICS2 are depicted in Figure 13. They are reconstructed according to the arrangement of these 25 pairs forming the IFU when the demodulation was performed after wavelength integration (binning) over the selected spectral lines. These maps provide an intuitive impression about the intensity and fractional linear polarization distribution. It is noteworthy that in these filter-like Q/I maps, the bright and dark square patches indicate the relatively strong positive and negative signals of polarizations, respectively, and the light gray patches mean zero or smaller amplitudes. Both I and Q/I maps of these two lines consistently provide information on the polarization distributions in the FOV: they are not spatially uniform, but highly structured, and the polarization planes experience irregular variations. On the other hand, although their intensity maps are very similar, the Q/I maps for these two lines are evidently different. This provides a clue to answer the question of which mechanisms produce the polarization.

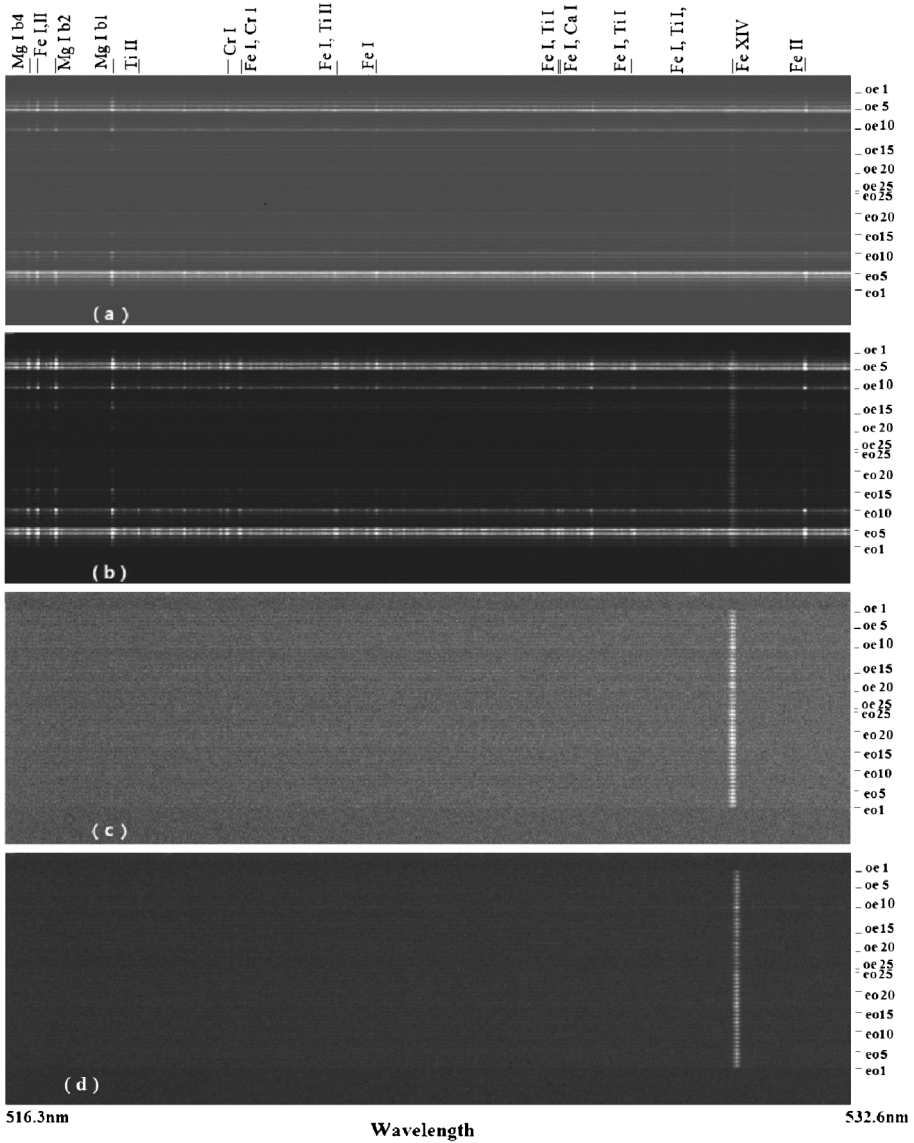


Figure 9 (a) and (b): Sample raw spectropolarimetric images acquired in the inner corona. (c) and (d): sample raw spectropolarimetric images of the outer coronal region. Note that in each panel the intensities of the upper 25 spectra are $1/2(I - Q)$ produced by *oe* pairs and the intensities of the lower 25 spectra are $1/2(I + Q)$ produced by *eo* pairs. The broad line in the right part that is present in all the frames is the famous green coronal line Fe XIV 530.3 nm. The alignments of the fiber pairs are labeled on the right.

4.2. Results from Polarimetric Observations of the Local Outer Corona

When the above calibrations and demodulations are applied to the outer coronal polarimetric measurement, the situation becomes more complicated. The most outstanding difference is that the continuum is beyond detection and the signal-to-noise ratio becomes much lower.

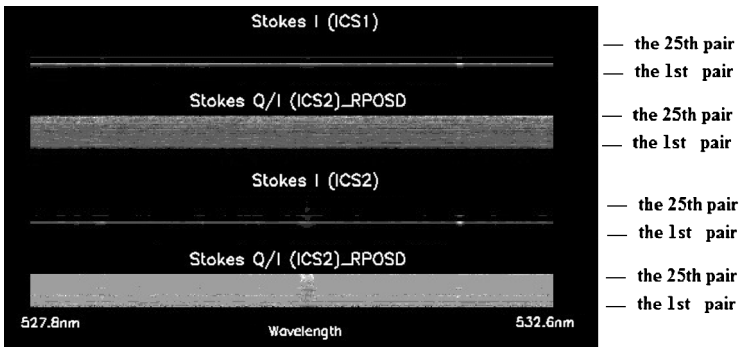


Figure 10 Stokes *I* spectral image and *Q/I* spectral images demodulated from the first (top panel, indicated by ‘ICS1’) and second (bottom panel, indicated by ‘ICS2’) inner coronal samples from the RPOSD. The alignment of the fiber pairs is indicated on the right.

By trial experiments, we found that it is crucial to exclude artificially high polarization degrees. For instance, a case leads to a fractional linear polarization of about 80.0 % when the ‘*oe*’ beam produces a readout of 18, and the ‘*eo*’ beam yields a readout of 2 after the dark-current and flat-fielding calibration. These false results are evidently induced by the noise fluctuations. In order to avoid any such an artificially high polarization due to the fluctuation of random photon noise, a threshold was set for both the ‘*oe*’ and ‘*eo*’ beam readouts below which the demodulation was abandoned and the polarization amplitude was set to be zero. In order to find a suitable threshold, we first measured the fluctuation in the upper and lower dark areas far away outside the regions covered by the spectrum in the raw polarimetric frames (*cf.* Figures 2 and 9) in terms of

$$rms = \sqrt{\Sigma_n (I(n) - \bar{I})^2 / n}, \tag{25}$$

where $I(n)$ and \bar{I} are the intensity readout for each pixel and the average value over these dark areas, respectively. The calculation leads to a fluctuation amplitude of about 6.5 in units of readout without pixel binning, sampled from OCS2 (lowest panels of Figure 9). For the 5×1 spatial binning adopted, the fluctuation becomes 19.3. Furthermore, a Gaussian distribution is assumed that leads to a threshold

$$I_{\text{threshold}} = e \times rms, \quad e = 2.71828. \tag{26}$$

Therefore, a cut-off threshold of 52.40 is adopted when the demodulation was processed.

The upper panel of Figure 14 displays the Stokes *I* and *Q/I* images demodulated from OCS1, and the lower part presents the demodulated results from OCS2 along with its following five frames within the same data set. Compared with the lower panel of Figure 10, a more complex distribution is shown. In Figure 15 a new pattern of profiles appears in which two opposite lobes are prominent, such as *Q/I* profiles produced from pairs 5 and 7. Again, the profile demodulated from pair 20 was found to belong to the most frequent pattern, and the complex configuration of profiles like the profile from pair 15 is the rarest.

On the other hand, we can see similarities among the six polarization images in the lower part of Figure 14 since they were acquired in nearly the same region within 48 seconds. In the following, we take the OCS2 as example that we discuss. At first glance, we show again that in the small FOV, both positive and negative polarizations are present alternatively, and this can also be seen from the *Q/I* maps in the lower row of Figure 17.

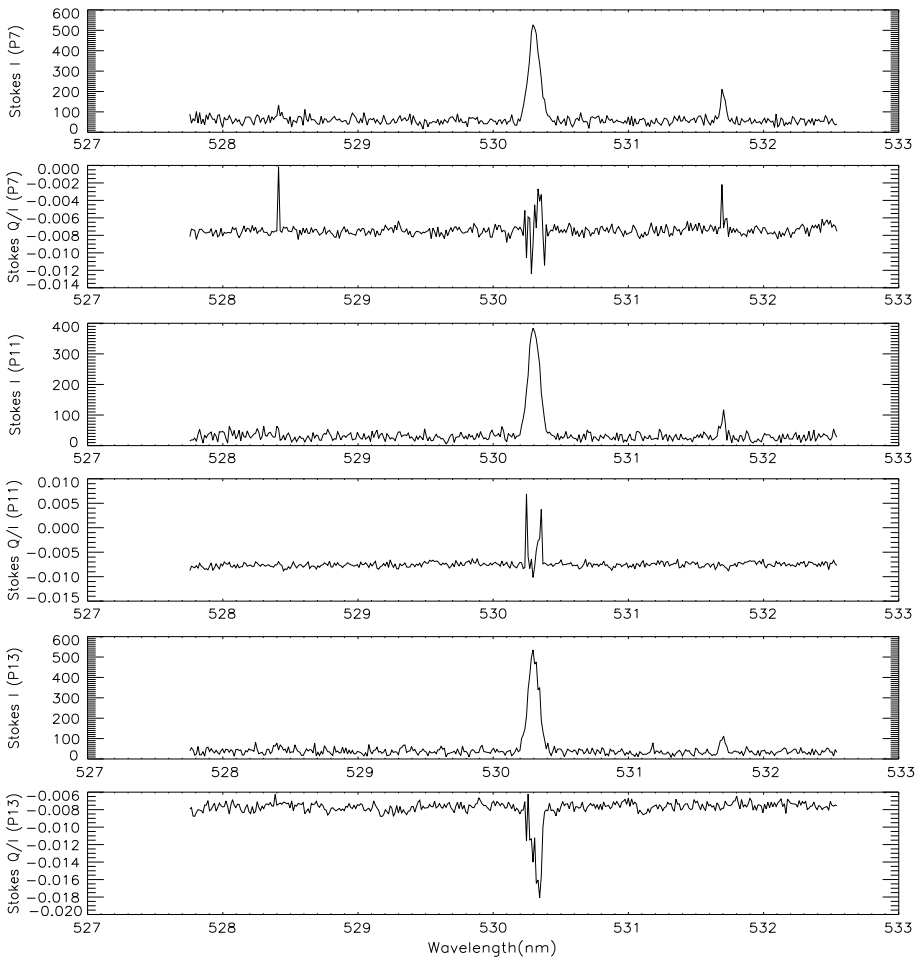


Figure 11 Stokes I and Q/I profiles yielded from the 7th, 11th and 13th pairs drawn from the lower panel of Figure 10.

In Figure 16 we plot three patterns of Q/I profiles, while all of Stokes I profiles appear to be single-peaked, like the pattern displayed in the top panel of Figure 15. As expected, the polarimetric noise level is greatly reduced compared with these noise levels shown in Figures 4, 5, 6, 7, 8 since the Moon by eclipsing the Sun decreased the scattered light in the sky. The greatest Q/I amplitude is detected to be about 3.2 % with respect to the continuum polarization level at the 24th pair (see the bottom curve of Figure 16). Combined with all the profiles displayed in Figures 11, 12, and 15, we find four types of profile configurations. They clearly show the diversity of the profile patterns. We now summarize these four categories in the demodulated assembly of Q/I profiles of the green coronal line, according to the following features of appearances:

1. Single-lobe dominated. A profile of this category has only one significant peak or valley. Examples are shown in the bottom panel of Figure 11 and in the second panel of Figure 15.

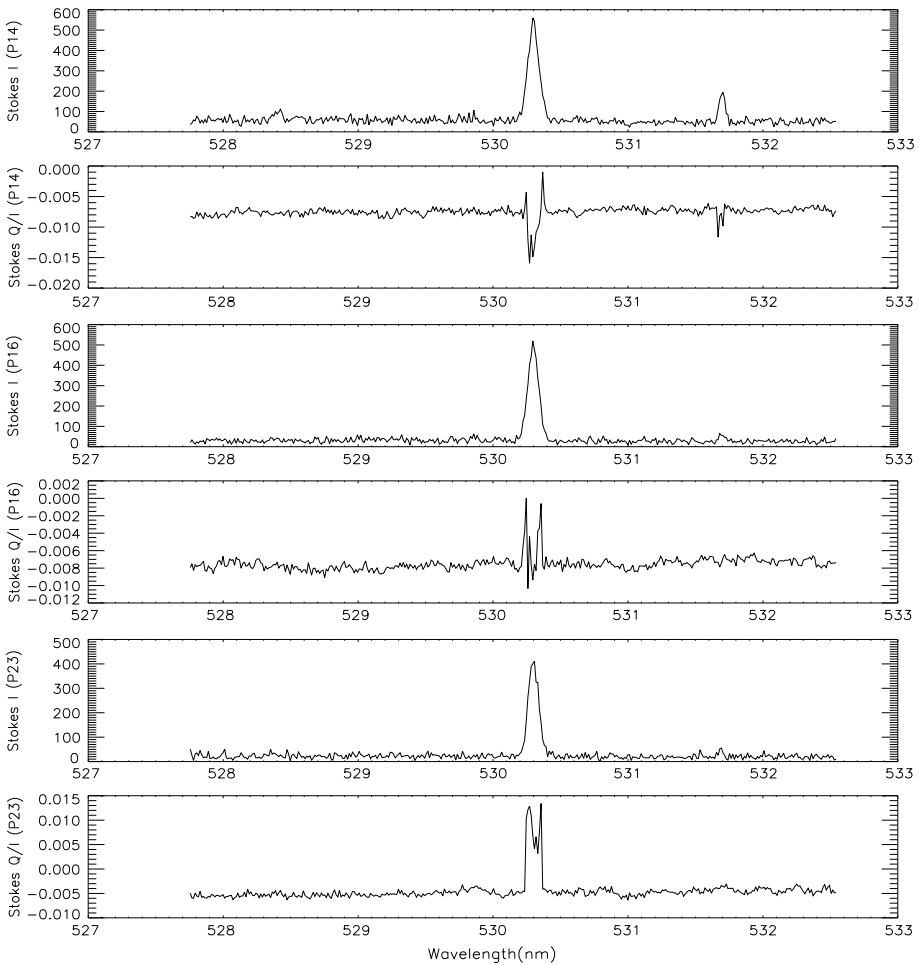


Figure 12 Stokes I and Q/I profiles yielded from the 14th, 16th and 23rd pairs drawn from the lower panel of Figure 10.

2. Dominated by two opposite lobes. Examples are shown in Figure 15, where pairs 5 and 7 yield this category of profiles, and the profile produced from pair 13 in Figure 16 is also typical of this type of profile.

3. Double significant lobes of the same sign with one valley or peak between them. This is the most frequent category in this polarimetric observation. Examples can be easily found in Figures 11, 12, 15, and 16.

4. Multiple lobes. This has the most complex appearance. Examples are the profile produced from pair 7 in Figure 11 and the profile from pair 15 in Figure 15.

The Stokes I and Q/I filter-like maps demodulated from these six frames containing OCS2 obtained by RPOSD after integration over the whole green coronal line are displayed in Figure 17. From Stokes I maps, an evident change can only be seen at the fifth frame, but the Q/I maps do not change significantly. This seems to indicate that no significant polarization variation with time occurred in this region during these acquisitions. This is not the case, however. In fact, the evolution was evident for each pair even from viewing

Figure 13 Stokes I and Q/I maps of the green coronal line (left column) and once ionized iron line Fe II 531.7 nm (right column), reconstructed from spatial binning and from demodulating the second inner coronal sample (ICS2).

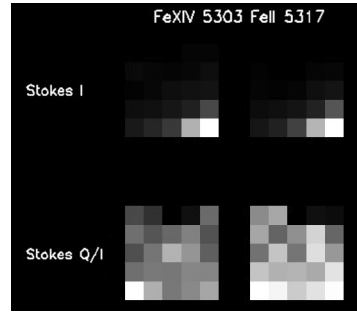
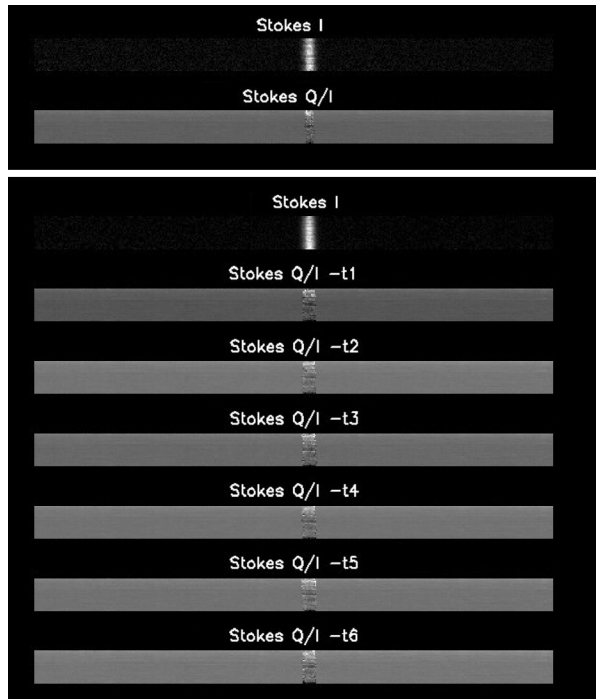


Figure 14 Stokes I and Q/I spectral images demodulated via RPOSD from the first outer coronal sample (OCS1, upper panel) and from the six frames of outer coronal sample data set containing the second outer coronal sample (OCS2, lower panel).



these spatially integrated Q/I profiles that are obtained by 25×5 binning over the 25 pairs of the whole FOV. Figure 18 displays these smoothed Q/I profiles obtained from the six frames. Five of the six profiles belong to the third category described above, but significant variations can be found in their amplitudes, while the last (sixth) profile is typical of the fourth category. This demonstrates that the filter-like Q/I maps cannot be used for very quantitative analysis. One important conclusion can be drawn that the spatial binning smears the details from the comparison of Figures 15 and 16 with Figure 18 and thus prevents us from understanding the mechanisms producing the polarization. Another fact is that the amplitude decreases greatly with the spatial integration. The greatest amplitude 0.31 % is found to be in the Stokes Q/I profile at $t3$, while 3.2 % results without the 25 spatial point binning. This is ascribed again to the dilution due to polarization plane variation and non-uniform amplitude distribution. Therefore, a high enough spatial resolution is necessary for coronal polarimetry.

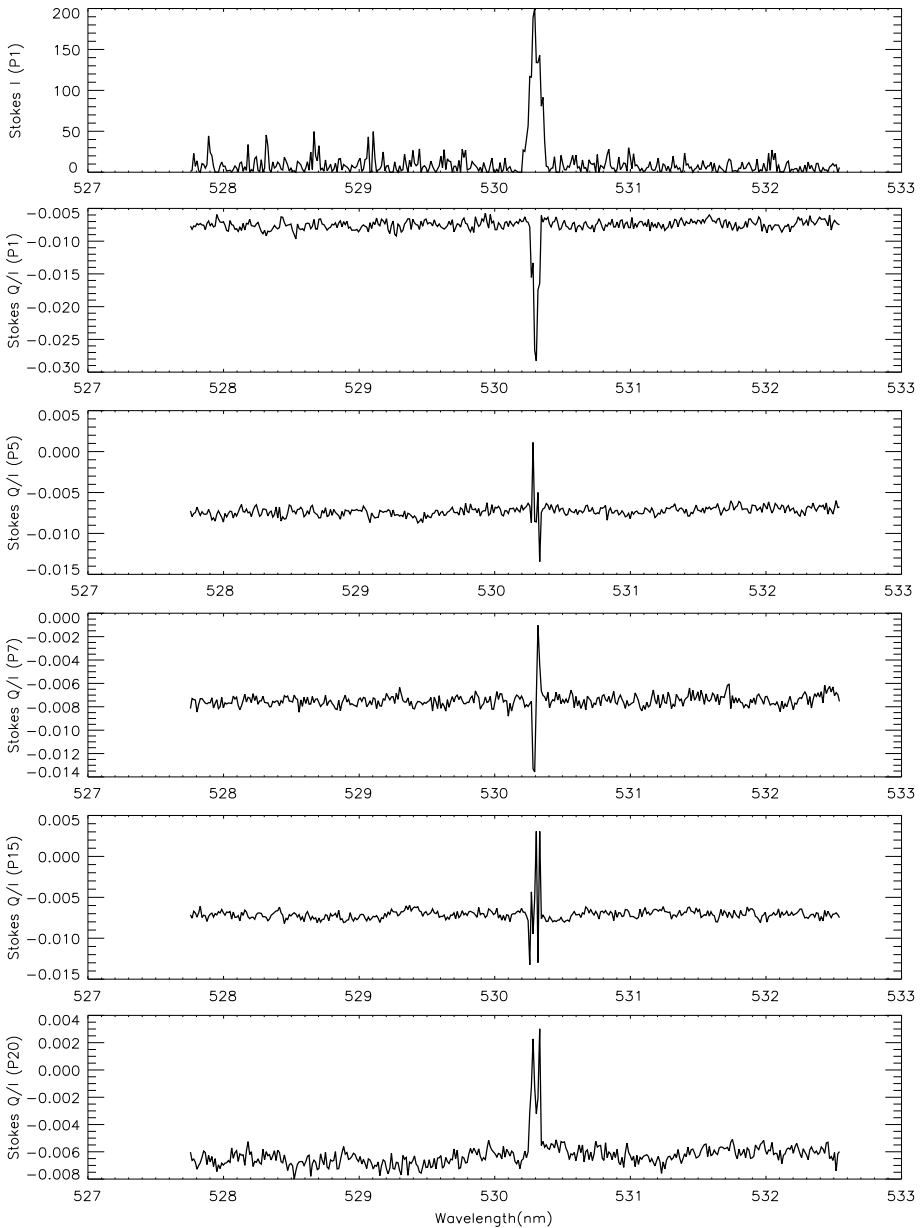


Figure 15 Sample Stokes I produced by pair 1 (uppermost panel) and Q/I profiles yielded respectively from pairs 1, 5, 7, 15 and 20 of OCS1.

5. Conclusions

We presented results from the spectro-imaging polarimetry (SIP) of the local solar corona during the 2013 total solar eclipse in Gabon. Compared with the former two flash spectropolarimetry measurements (Qu *et al.*, 2009, 2013), the present polarimetric observation

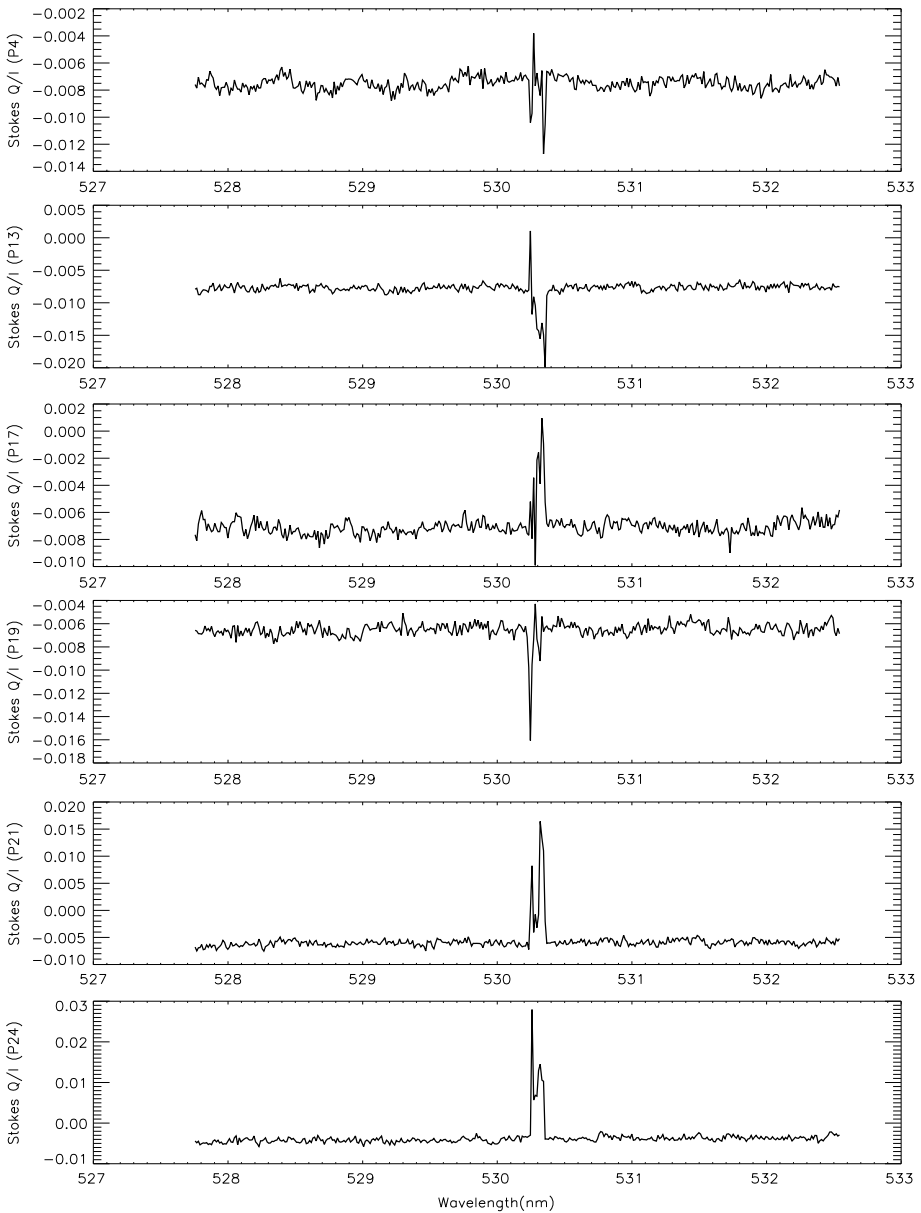


Figure 16 Sample Stokes Q/I profiles yielded from pairs 4, 13, 17, 19, 21, and 24 of OCS2.

has been improved considerably in the following two aspects. First, it is capable of spectro-imaging polarimetry for the first time, which was enabled by adopting the IFU pair technique. The imaging-polarimetry with rough spectral resolution, for instance, the bandpass comparable to the spectral line width, may not only blur the spectral details, but also leads to a greatly reduced polarization degree if the profile contains lobes with opposite signs, like the second and fourth categories of Stokes Q/I profile described in the section above.

Figure 17 Stokes I and Q/I maps of the green coronal line reconstructed from the six frames (labeled by t_1 to t_6) containing OCS2.

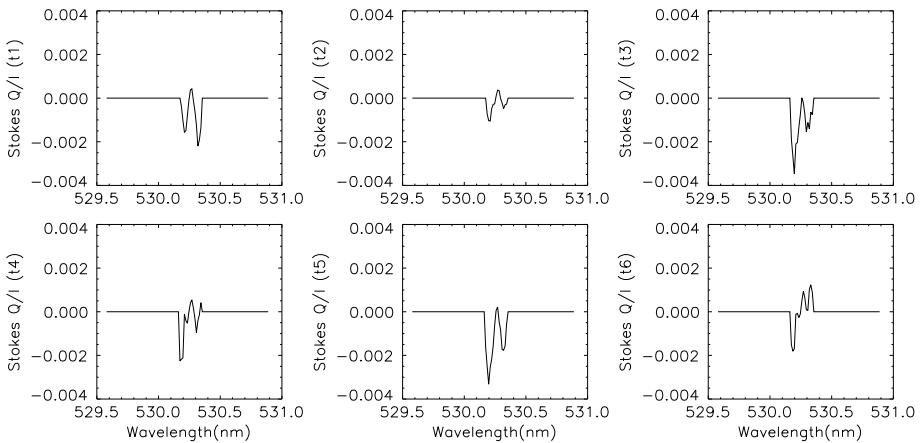
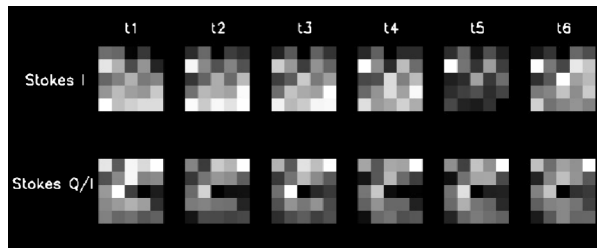


Figure 18 Spatially integrated Stokes Q/I profile evolution demodulated from the second outer coronal sample data set after spatial binning of all the 25 fiber pairs.

Second, the polarimetric noise level has been decreased by one order by applying the Reduced Polarimetric Optical Switching (RPOSD). The observation mode based on this demodulation procedure can increase the temporal resolution twice compared to those based on the classical POS performance and save document storage space if the acquisitions are massive.

To conclude, we showed that spectro-imaging polarimetry of the green coronal line has revealed new interesting features of the solar corona. In particular, three observations should be highlighted:

1. Although the fractional linear polarization of coronal radiation can only reach 3.2 % on a scale of 1500 km, we found that the polarization distribution is very localized in the inner corona but more universal in the outer corona.

2. Even within one small FOV, the polarization distribution is non-uniform on a small scale. For instance, the amplitude of 3.2 % on a scale of 1500 km decreased to 0.31 % on a scale of 7500 km. This is partially due to spatial dilution in the inner corona, but also to the polarization plane variation within the FOV. This tells us that coronal polarimetry needs high spatial resolution if the mechanisms are to be revealed. However, in contrast, the continuum polarization seems unchanged with height with a value of -0.74 % in the inner corona.

3. The demodulated Q/I profiles exhibit abundant patterns on a scale of two arcseconds. We have classified these patterns into four categories. This may indicate that the polarization profiles are formed by not only anisotropic scattering and other physical mechanisms, but also by complex motion patterns of the plasma along the line of sight.

As a closing remark, because total solar eclipses on the ground are rare, a satellite-borne coronagraph focusing on high spectral and spatial resolution spectro-imaging polarimetry of the solar corona is strongly recommended to routinely execute the polarimetric observation with considerable spatial resolution. We wish that this may open a window for advanced solar coronal polarimetry.

Acknowledgements This work is sponsored by the National Science Foundation of China (NSFC) under the grant numbers 11373065, 11527804, 11078005, 10943002, and by the Natural Scientific Foundation of Yunnan province under grant number 2010CD113.

Disclosure of Potential Conflicts of Interest The authors declare that they have no conflicts of interest.

Open Access This article is distributed under the terms of the Creative Commons Attribution 4.0 International License (<http://creativecommons.org/licenses/by/4.0/>), which permits unrestricted use, distribution, and reproduction in any medium, provided you give appropriate credit to the original author(s) and the source, provide a link to the Creative Commons license, and indicate if changes were made.

References

- Allington-Smith, J., Murray, G., Content, R., Dodsworth, G., Davies, R., Miller, B.W., *et al.*: 2002, *Publ. Astron. Soc. Pac.* **114**, 892. [DOI](#)
- Badalyan, O.G., Sýkora, J.: 1997, *Astron. Astrophys.* **319**, 664.
- Bianda, M., Solanki, S.K., Stenflo, J.O.: 1998, *Astron. Astrophys.* **331**, 760.
- Blackwell, D.E., Petford, A.D.: 1966, *Mon. Not. Roy. Astron. Soc.* **131**, 399.
- Dai, X., Wang, H., Huang, X., Du, Z., He, H.: 2015, *Astrophys. J.* **801**, 39. [DOI](#)
- Donati, J.-F., Semel, M., Rees, D.E., Taylor, K., Robinson, R.D.: 1990, *Astron. Astrophys.* **232**, L1.
- Eddy, J.A., McKim Malville, J.: 1967, *Astrophys. J.* **150**, 289.
- Feller, A., Ramelli, R., Stenflo, J.O., Gisler, D.: 2007, *ASP Conf. Ser.* **368**, 627.
- House, L.L.: 1977, *Astrophys. J.* **214**, 632.
- House, L.L., Querfeld, C.W., Rees, D.E.: 1982, *Astrophys. J.* **255**, 753.
- Hyder, C.L., Mauter, H.A., Shutt, R.L.: 1968, *Astrophys. J.* **154**, 1039.
- Koutchmy, S., Schatten, K.H.: 1971, *Solar Phys.* **17**, 117. [DOI](#)
- Kulijanishvili, V.I., Kapanadze, N.G.: 2005, *Solar Phys.* **229**, 45. [DOI](#)
- McDougal, D.S.: 1971, *Solar Phys.* **21**, 430. [DOI](#)
- Molodensky, M.M.: 1973, *Solar Phys.* **28**, 465. [DOI](#)
- Ney, E.P., Huch, W.F., Kellogg, P.J., Stein, W., Gillett, F.: 1961, *Astrophys. J.* **133**, 616. [DOI](#)
- Qu, Z.Q.: 2011, *ASP Conf. Ser.* **437**, 423.
- Qu, Z.Q., Chang, L., Cheng, X.M., Allington-Smith, J., Murray, G., Dun, G.T., Deng, L.H.: 2014, *ASP Conf. Ser.* **489**, 263.
- Qu, Z.Q., Deng, L.H., Dun, G.T., Chang, L., Zhang, X.Y., Cheng, X.M. *et al.*: 2013, *Astrophys. J.* **774**, 71.
- Qu, Z.Q., Zhang, X.Y., Xue, Z.K., Dun, G.T., Zhong, S.H., Liang, H.F., *et al.*: 2009, *Astrophys. J.* **695**, L194.
- Raouafi, N.-E.: 2005, In: Innes, D.E., Lagg, A., Solanki, S.K., Danesy, D. (eds.) *Proceedings of the International Scientific Conference on Chromospheric and Coronal Magnetic Fields, ESA SP-596*, 3.
- Raouafi, N.-E.: 2011, *ASP Conf. Ser.* **437**, 99.
- Raouafi, N.-E., Lemaire, P., Sahal-Bréchet, S.: 1999, *Astron. Astrophys.* **345**, 999.
- Raouafi, N.-E., Sahal-Bréchet, S., Lemaire, P.: 2002, *Astron. Astrophys.* **396**, 1019.
- Raouafi, N.-E., Solanki, S.K.: 2003, *Astron. Astrophys.* **412**, 271.
- Skomorovsky, V.I., Trifonov, V.D., Mashnich, G.P., Zagaynova, Y.S., Fainshtein, V.G., Kushtal, G.I., Chuprakov, S.A.: 2012, *Solar Phys.* **277**, 267. [DOI](#)
- de Wijn, A.G., Tomczyk, S., Burkepile, J.: 2014, *ASP Conf. Ser.* **489**, 323.
- Trujillo Bueno, J.: 2010, In: Hasan, S.S., Rutten, R.J. (eds.) *Magnetic Coupling Between the Interior and Atmosphere of the Sun Astrophys. Space Sci. Proc.* Springer, Berlin, Heidelberg, 118. [DOI](#)